RESEARCH ARTICLE

Bioinspired 3D microprinted cell scaffolds: Integration of graph theory to recapitulate complex network wiring in lymph nodes

Matthew H. W. Chin[1] | Barry Reid[1] | Veronika Lachina[2] | Sophie E. Acton[2] | Marc-Olivier Coppens[1]

[1]EPSRC "Frontier Engineering" Centre for Nature-Inspired Engineering (CNIE) and Department of Chemical Engineering, University College London, Torrington Place, London, UK

[2]Stromal Immunology Group, MRC Laboratory for Molecular Cell Biology, University College London, London, UK

Correspondence
Marc-Olivier Coppens, EPSRC "Frontier Engineering" Centre for Nature-Inspired Engineering (CNIE) and Department of Chemical Engineering, University College London, Torrington Place, London, WC1H 0AJ, UK.
Email: m.coppens@ucl.ac.uk

Abstract

Physical networks are ubiquitous in nature, but many of them possess a complex organizational structure that is difficult to recapitulate in artificial systems. This is especially the case in biomedical and tissue engineering, where the microstructural details of 3D cell scaffolds are important. Studies of biological networks—such as fibroblastic reticular cell (FRC) networks—have revealed the crucial role of network topology in a range of biological functions. However, cell scaffolds are rarely analyzed, or designed, using graph theory. To understand how networks affect adhered cells, 3D culture platforms capturing the complex topological properties of biologically relevant networks would be needed. In this work, we took inspiration from the small-world organization (high clustering and low path length) of FRC networks to design cell scaffolds. An algorithmic toolset was created to generate the networks and process them to improve their 3D printability. We employed tools from graph theory to show that the networks were small-world (omega factor, $\omega = -0.10 \pm 0.02$; small-world propensity, SWP = 0.74 ± 0.01). 3D microprinting was employed to physicalize networks as scaffolds, which supported the survival of FRCs. This work, therefore, represents a bioinspired, graph theory-driven approach to control the networks of microscale cell niches.

KEYWORDS

additive manufacturing, algorithmic design, bioengineering, biomaterials, nature inspired engineering

1 | INTRODUCTION

3D cell scaffolds used in tissue engineering and disease modelling are typically modelled after structurally complex fibrous or porous networks in natural tissue microenvironments, such as the extracellular matrix (ECM).[1–3] Lately, modelling efforts have broadened to encompass the lymph node, a crucial organ of which there are hundreds dispersed across the lymphatic system. Lymph nodes act as information-exchange hubs for immune cells. Gaining insights into their functions could improve our understanding of immune response regulation and disorders including cancer.[4] This has motivated the development of biomaterial-based models like hydrogels, organoids, and organ chips, which enable the isolation and examination of single factors—an infeasible endeavor with animal models.[5] However, prevailing biomaterial models fall short in recapitulating the complex geometry of the lymph node microenvironment. Specifically, networks

formed by fibroblastic reticular cells (FRCs) in the lymph node act as "highways" supporting the navigation of immune cells. Yet, exploration of their geometry has, so far, been limited to mathematical or in silico modelling. Here, we present a novel, manufacturability-focused approach, rooted in graph theory and enabled by 3D microprinting, to fabricate biomaterial scaffolds that mirror the complex wiring of FRC networks.

In the last two decades, many of these cell scaffolds were fabricated using non-digital methods, including porogen leaching, phase separation and electrospinning.[6] Nevertheless, such methods offer limited control over the scaffold microarchitecture, which is known to critically regulate a myriad of cell functions, including migration, proliferation, differentiation, and morphology.[7,8] In recent years, the challenge of controlling microarchitecture has been tackled through advances in 3D microprinting. One of the well-known approaches relies on laser-induced two-photon polymerization (2PP) of photosensitive resins.[9,10] Using 2PP-based direct laser writing (DLW), scaffolds can be created with submicron resolution, as polymerization events are confined to the small (~nm) focal region of an ultrafast pulsed laser beam. This fabrication technique has enabled the creation of structures for a range of engineering applications, including cell scaffolds,[11] mechanical metamaterials,[12] as well as photonic crystals.[13]

Current scaffolds fabricated by 2PP DLW tend to have a highly ordered, periodic structure composed of repeating unit cells. Much focus has been placed on the exact arrangement, geometry, and topology of the individual unit cells. As such, these structures were determined a priori within computer-aided design (CAD). To date, many 2PP DLW cell scaffolds assume a woodpile structure consisting of rods, bars or beams stacked on top of each other, but their network topologies do not necessarily reflect that of the modelled microenvironment.[14] In contrast, structures with random or disordered networks have not been as widely explored, despite their advantages in mechanical metamaterial design [15] and biomaterials modelling.[16] Furthermore, many complex biological networks, such as the ECM and cytoskeleton, do not possess the regularity of these common CAD models.[17,18] Taken together, a question arises as to how complex network architecture should be incorporated into scaffold CAD models for 2PP DLW.

Addressing the challenge, an algorithmic design approach can be derived from graph theory, where CAD models are generated based on network construction rules. Watts and Strogatz demonstrated in their seminal 1998 paper that the topological properties of many real-world networks (in social, technological, and biological systems) are neither completely ordered nor completely random.[19] These networks are known to exhibit the so-called "small-world" organization, with small average shortest path length and high clustering. Furthermore, Watts and Strogatz showed that small-world networks can be created by introducing shortcuts via partial, random rewiring of a lattice network. A notable feature of such a network architecture is that it can minimize wiring and energetic costs, while maximizing information propagation across the network.[20] In addition to the classic Watts-Strogatz model, there is a variety of generative models that can also form small-world networks, based on spatial distances between nodes—in graph theory,

networks generated in this fashion are known as random geometric graphs (RGGs).[21,22]

With growing availability of spatial data, graph theory is increasingly employed to characterize various kinds of interconnected cellular networks. Such networks—known as "cell graphs" [23]—have contributed to the emergence of connectomics and computational methods for histopathological image classification, such as "tumor graphs."[24] These include not only widely studied neural circuits in the brain, but also osteocyte networks in the mineralized bone matrix and FRC networks in lymph nodes, which have all been reported to be small-world.[25–28] Here, the revelation of lymph node FRC network topology is particularly interesting and timely because it coincides with the current rise of cancer immunotherapies. The crucial role that FRC networks play in regulating immune cells in both homeostasis and immune responses prompts for new cross-disciplinary enquiries [4]— for example, the impact of small-world topology on T cell migration, and its implications for emerging cancer therapies, such as chimeric antigen receptor (CAR) T cell therapies.[29] Nevertheless, cell scaffolds designed based on graph theory are rare, let alone those specifically designed to have a small-world structure.

In this work, we employed a nature-inspired solution (NIS) methodology (Figure 1) to integrate graph theoretic tools, algorithmic design, and 3D micro-printing within a systematic framework to create 3D microprinted scaffolds.[30] We took inspiration from the lattice-like, small-world properties of FRC networks and used them as constraints in our computational model to generate lymph node-inspired RGG networks. In the generation process, we encountered two main technical challenges—intersecting edges and floating islands. The former would make the resulting 3D structure topologically inaccurate, and the latter would render it unprintable. We therefore extended the original generative model to include operations correcting for these artefacts. Network analysis revealed that the generated networks displayed small-world characteristics comparable to those of FRC networks. As a proof-of-concept, we demonstrated the applicability of the scaffolds as an in vitro cell culture platform by seeding them with FRCs to examine their ability to support cell survival and cell-material interactions.

2 | MATERIALS AND METHODS

2.1 | Algorithmic design

The overall design approach is depicted in Figure 2. Scaffolds were generated using Grasshopper (v1.0.0007), an algorithm editor integrated with tools in the CAD application, Rhino 7 (Robert McNeel & Associates). Lists of Grasshopper libraries and components used are provided in the supplementary material (Table S1 and S2). Videos of the generation process are also available (Video S1-S4). The algorithm for scaffold generation is available on GitHub (https://github.com/mattychin/3D-cell-scaffold-generator).

To begin, 65 nodes were generated uniformly at random within a 3D space of $100 \times 100 \times 100~\mu m^3$. The number of nodes was chosen based on the node density determined from a previously reported
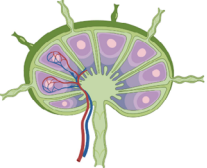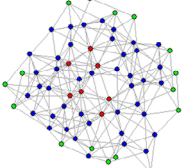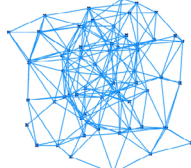
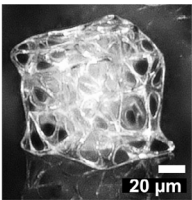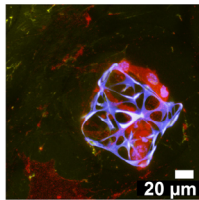| Mechanism	Nature	Nature-inspired concept	Nature-inspired design	Prototype/ experimental realization	Application
Ecosystems, networks and modularity	FRC networks in secondary lymphoid organs	Small-world topology	Algorithmically generated spatial network	3D microprinted scaffold	*In vitro* 3D cell culture platform

FIGURE 1 Nature-inspired solution (NIS) methodology: the present work takes inspiration from the topology of FRC networks to create small-world spatial networks through algorithmic design. The networks are physicalized as 3D microscale scaffolds using additive manufacturing (2PP DLW) and can be used as an in vitro 3D culture platform for mammalian cells.
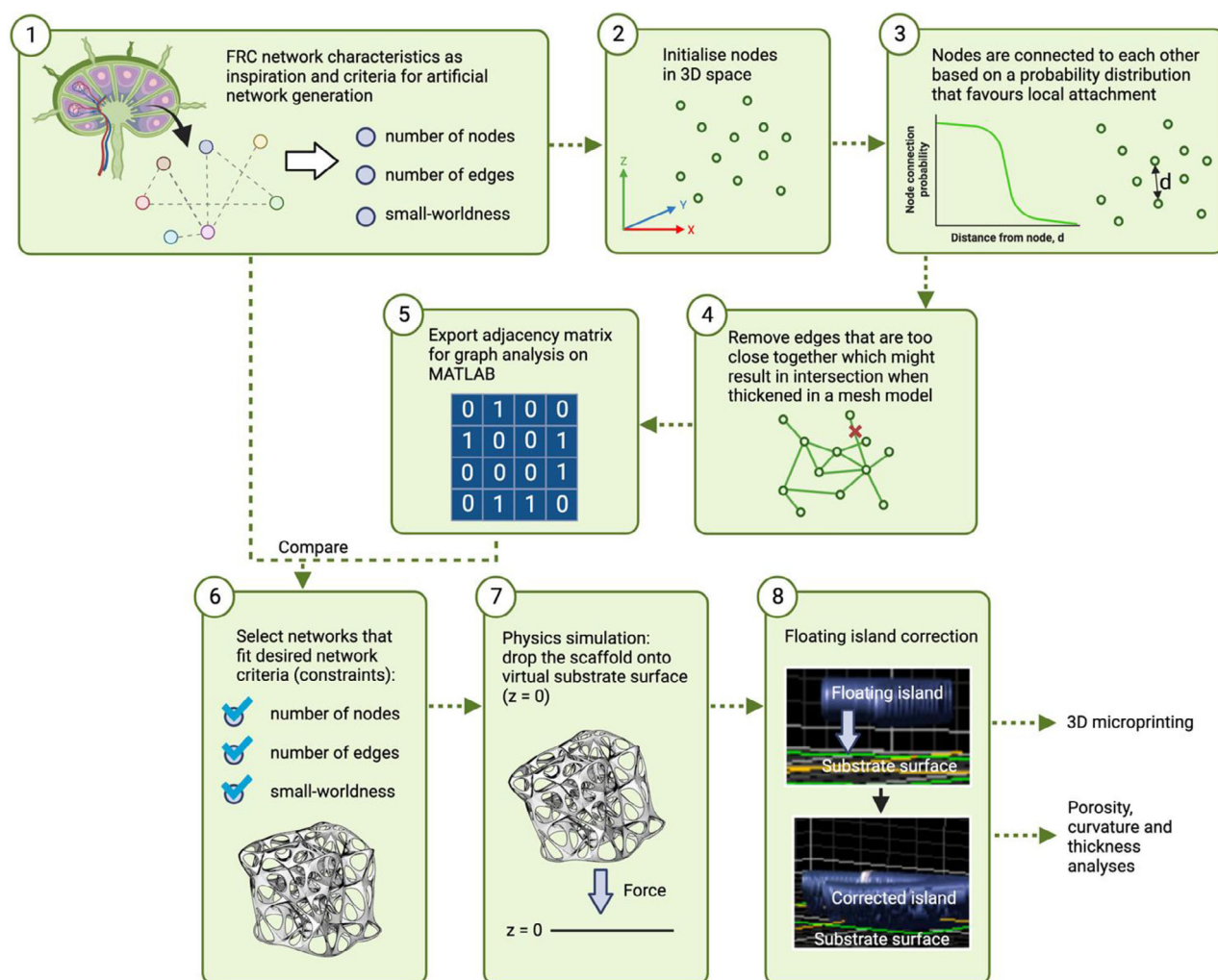

FIGURE 2 Algorithmic design approach employed to generate 3D scaffolds. (1) Taking inspiration from FRC networks, the topological characteristics were used as constraints in our model. (2) Nodes were randomly generated within a 3D simulation space and then (3) connected based on a probability distribution. (4) Intersecting edges were removed. (5) Adjacency matrices specifying connections in the generated networks were then exported to MATLAB for analysis. (6) Networks that fit the design criteria were then selected for further processing. To make the scaffolds 3D printable, they were modified to (7) make contact with the substrate surface and (8) eliminate floating islands. The resulting CAD models were then used for downstream characterization (curvature, porosity, and thickness) and 3D microprinting.

study, where 176 FRCs were identified within a representative image slice ($300 \times 300 \times 30 \ \mu m$) of a murine lymph node[34]. In Grasshopper, the nodes were connected based on a soft RGG model utilized by Soekarjo et al. for small-world network generation that preferentially connects nodes close to each other.[31] The model specifies the internodal distance probability distribution as a Hill-type function:

$$p\ (d) = \begin{cases} \dfrac{1}{1+\left(\frac{d}{k}\right)^m}, & d \leq l \\ 0, & otherwise \end{cases} \tag{1}$$

where d is the distance between any two nodes, m modulates the steepness of the curve, l is the maximum distance for connection, and k is the distance at which the probability for connection, $p(d)$, is half maximal. The resulting function assumes a sigmoidal shape where the probability for connection decreases as d increases. The RGG generated from such probabilistic connection function is known as a soft RGG, as it has two sources of randomness—position of nodes and formation of edges. The algorithm looped through all node pairs and, if the pair satisfied the condition $d < l$, a connection probability was calculated. While networks were created using different combinations of m and k, we kept l fixed at $75 \ \mu m$, a maximum FRC connection length that has been reported previously [32] and was also used in models.[31] After looping through the nodes, the collection of generated edges formed the skeleton of the scaffold.

To create a 3D printable object, the generated skeleton was skinned with a mesh, using the Fattener plugin by Daniel Piker (documentation available in link, Table S2), and then smoothed with Catmull-Clark subdivision (Weaverbird plugin). The resulting scaffold model was modified to remove edges that were intersecting, or too close to, each other (Video S2). This was done by assigning equally spaced sampling points along the length of each edge and measuring the distances from points on one edge to those on another. If an edge was $< 5 \ \mu m$ from a neighboring edge, then the edge that was generated later would get removed. The $5 \ \mu m$ threshold was chosen to avoid edge-edge or edge-node intersections after mesh application. This essentially forbade the formation of a new edge if there was already a pre-existing edge in the way.[40,41]

The 2PP method was employed to fabricate scaffolds on a glass slide in an upside-down configuration. Therefore, it was crucial to ensure that the base layer of the CAD model contacted the substrate ($z = 0$). To increase the number of contact points with the substrate, the scaffold was "dropped" onto the x-y plane using the FlexHopper physics engine to simulate gravity and collisions in Grasshopper (Video S3). Both the scaffold and x-y plane were specified as colliders in the simulation, but the distance that objects should maintain from each other was deliberately not specified, such that the plane would intersect the scaffold slightly upon collision. This intersection was then utilized to trim the bottom of the scaffold mesh to ensure it had a flat interface with the substrate.

To remove floating islands in the CAD model, we created an algorithm to detect isolated meshes that were above the x-y plane (Video S4). The vertices of isolated meshes were then translated to the plane,

TABLE 1 Fabrication parameters for scaffold 3D microprinting.

Resin	IP-Dip
Slicing mode	Fixed
Slicing distance (μm)	0.2
Hatching distance (μm)	0.1
Laser power (%)	50–85
Laser scan speed ($\mu m \ s^{-1}$)	8000–10,000

where the mesh face was rebuilt. This operation essentially stretched the bottom portion of the mesh model to contact the plane.

2.2 | 3D microprinting

3D models were exported from Rhino as Standard Triangle Language (STL) files and imported into the Nanoscribe software package, DeScribe, which creates the General Writing Language (GWL) job files specifying the printing parameters (Table 1). The GWL files were imported into another Nanoscribe software package, NanoWrite, to execute the printing.

Microscale scaffolds were fabricated using the 2PP DLW method with a Nanoscribe Photonic Professional GT system in dip-in laser lithography (DiLL) configuration, with a 63× objective featuring 1.4 numerical aperture. In DiLL, the objective lens was in direct contact with the photoresist to reduce optical aberrations. The Nanoscribe system uses two coupled galvanometric mirrors to scan the laser beam in the x- and y- directions, while a piezoelectric stage, as well as the built-in z drive of the objective, are used for movements in the z-direction.

Before printing, fused silica substrates were washed with acetone, followed by isopropanol, and then dried under a stream of nitrogen gas. The Nanoscribe system relies on refractive index contrast to find the interface between the photoresist and substrate. For this reason, structures were fabricated on fused silica substrates. To facilitate scaffold-substrate adhesion, the substrates were exposed to oxygen plasma (Henniker Plasma HPT-100) at 100 W for 1 min. We chose IP-Dip (Nanoscribe) as the 3D printing resin because it is a commercial resin widely used for high-resolution printing. The resin is a proprietary negative-tone photoresist (consisting primarily of pentaerythritol triacrylate [33]) known to be biocompatible.[34] The IP-Dip was cast on fused silica substrates ($25 \ mm \times 25 \ mm$, thickness = $0.7 \ mm$; Nanoscribe) before insertion into the Nanoscribe system. To remove unpolymerized resin after fabrication, the structures were developed in propylene glycol monomethyl ether acetate (ReagentPlus grade: ≥ 99.5%; Merck Sigma-Aldrich) for 20 min, followed by IPA (≥ 99.5%; Merck Sigma-Aldrich) for 5 min, and then dried under a stream of nitrogen gas.

Images of 3D prints were acquired using a Keyence digital microscope (VHX-7000). For clarity, the "live depth composition" function was used to create a single, fully focused image from images automatically captured at different focal planes. To obtain a tilted view of the

scaffolds, the microscope head was rotated 65° before running the live depth composition scan.

2.3 | 3D printing macroscale models

To visualize intersecting edges more easily, macroscale scaffolds were created via selective laser sintering (SLS) of Nylon 12 (PA 2200) powder using an EOS Formiga P100 3D printer. The bounding box dimensions for the printed scaffolds were 79.9 mm × 79.3 mm × 78.0 mm for the original scaffold and 79.9 mm × 80.1 mm × 76.9 mm for the modified scaffold. A wrap operation (radial offset of 0.5 mm) was also applied to thicken the scaffolds such that they could withstand the printing and cleaning process.

2.4 | Network analysis

The adjacency matrix of each Grasshopper-generated network was created using the library SpiderWeb. Network analysis was performed using MATLAB (vR2022b). "Small-worldness" of the networks was quantified using the omega factor (ω) [35] and small-world propensity (SWP).[26] MATLAB functions from the Brain Connectivity Toolbox (BCT; http://www.brain-connectivity-toolbox.net) were adapted to calculate clustering coefficients and ω. SWP values were calculated using a MATLAB function obtained from the Network Community Toolbox (http://commdetect.weebly.com/).[26] An additional small-world index, the sigma factor (σ), was also calculated for generated networks and values are available in Table S3-4. A comprehensive description of each small-world index has been provided by Nokovic et al., in their analyses of FRC networks.[27,28] Networks are considered small-world if $-0.5 < \omega < 0.5$ and $\sigma > 1$. In terms of SWP, networks are in the "strong" small-world regime if SWP ≥ 0.6. The small-world indices are defined as follows:

$$\omega = \frac{L_R}{\bar{L}} - \frac{\bar{C}}{C_L}, \quad -1 \leq \omega \leq 1 \tag{2}$$

$$\sigma = \frac{\bar{C}/C_R}{\bar{L}/L_R}, \quad 0 \leq \sigma < \infty \tag{3}$$

$$SWP = 1 - \sqrt{\frac{\Delta_C^2 + \Delta_L^2}{2}}, \quad 0 \leq SWP \leq 1 \tag{4}$$

Here, the clustering coefficient ratio, $\Delta_C = \frac{C_L - \bar{C}}{C_L - C_R}$ and the shortest path length ratio, $\Delta_L = \frac{\bar{L} - L_R}{L_L - L_R}$. $\bar{C}$, C_L, and C_R are the average local clustering coefficients of the empirical network, equivalent lattice network and equivalent random network, respectively. $\bar{L}$, L_L and L_R are the shortest path lengths of the empirical network, equivalent lattice network and equivalent random network, respectively. The synthetic benchmark networks (random and lattice) used for the calculation of C_L, C_R, L_L, and L_R were generated using the BCT.[36,37]

The local clustering coefficient, c_i, of a node, i, with k_i neighbors (where $k_i > 1$), is defined as the ratio of the actual number of edges, e_i, among neighbors of i, to the maximum attainable number of edges among its neighbors [19]:

$$c_i = \frac{2e_i}{k_i(k_i - 1)}, \quad 0 \leq c_i \leq 1 \tag{5}$$

The average local clustering coefficient, $\bar{C}$, of a network with N nodes is the arithmetic mean of the local clustering coefficients:

$$\bar{C} = \frac{1}{N} \sum_{i=1}^{N} c_i, \quad 0 \leq \bar{C} \leq 1 \tag{6}$$

The average shortest path length, $\bar{L}$, of a network is the arithmetic mean of all pairs of geodesic distances between nodes i and j:

$$\bar{L} = \frac{2}{N(N-1)} \sum_{i=1}^{n} \sum_{j=i+1}^{n} l_{ij}, \quad 1 \leq \bar{L} < \infty \tag{7}$$

where l_{ij} is the shortest path length between node i and node j (minimum number of edges required to get from node i to node j).

Scaffold networks (original and modified) were further compared with equivalent graphs—Watts-Strogatz (WS) small-world,[19] ring lattice and Erdős-Rényi random networks.[38] WS networks were generated with rewiring probability, $p = 0.14$. This probability was chosen to approximate an equivalent WS network with a mean omega factor (ω) close to zero, where small-worldness is considered the greatest (Table S5). Ring lattices were generated by connecting each node to four neighbors. Erdős-Rényi random networks were constructed using the igraph package (v1.3.5) on R (v4.2.1) as graphs with 65 nodes and 253 edges, which were selected uniformly at random from the set of all possible edges.

To examine how model parameters m and k in **Equation (1)** could influence the number of generated edges, a one-at-a-time sensitivity analysis was performed using MATLAB. The sensitivity index for m and k values was computed by dividing the difference in the number of edges between adjacent values of m and k by the number of edges for the previous value. A heatmap of the sensitivity index for each parameter was plotted, with the color representing the magnitude and sign of the sensitivity index. The color scale ranges from -1 to 1, where negative values indicate a decrease in the number of edges and positive values indicate an increase in the number of edges when the corresponding parameter is increased.

2.5 | 3D cell culture

Cell culture chambers were constructed by integrating scaffold-decorated fused silica glass slides with MatTek bottomless culture dishes (MatTek corporation) using polydimethylsiloxane (PDMS) from a Sylgard 184 silicone elastomer kit at a monomer-to-crosslinker ratio of 10:1. The PDMS was allowed to cure overnight at room temperature. Scaffold arrays were then rinsed three times in phosphate buffered saline (PBS; ThermoFisher) to remove any residue that had not been polymerized and to ensure a leak-free seal was formed. For cell adhesion, the arrays were coated with soluble human fibrinogen (Fisher

Scientific) at $50\,\mu g\,mL^{-1}$ and human fibronectin (Merck) at $50\,\mu g\,mL^{-1}$ by physisorption for 2.5 h at 37°C. Excess protein was removed by washing three times with PBS and the scaffolds were sterilized in ultra-violet light for 30 min at room temperature. The arrays were then stored in sterile PBS at 4°C until use. Immortalized FRCs expressing cytoplasmic mOrange [39] were used to seed the scaffolds. 1×10^5 FRCs were applied to the scaffolds in $500\,\mu L$ Dulbecco's Modified Eagle Medium (DMEM) containing 10% foetal bovine serum and incubated for 1 h at 37°C. The scaffolds were then washed with PBS to remove non-adhered cells and then kept in DMEM at 37°C and 10% CO_2 until imaging.

2.6 | Cell imaging

Live cells (day 3) and fixed cells (day 4) were imaged using a Zeiss LSM 880 inverted multiphoton microscope, equipped with a W Plan-Apochromat ×40 water-dipping objective (NA 1.0). Cells were fixed with 3.7% formaldehyde for 10 min and then washed twice with PBS. The cells were then permeabilized in PBS containing 0.2% Triton-X100 for 10 min at room temperature before washing twice with PBS. Subsequently, the cells were incubated in 2% bovine serum albumin (BSA; Sigma-Aldrich, a2153)/PBS for 1 h at room temperature for blocking. The BSA was aspirated and the cells were stained with TRITC-phalloidin (Sigma, p1951) to reveal F-actin in 500 mL of 2% BSA/PBS for 1 h. Fiji (ImageJ) was used to create z projections (sum of intensities) from z-stack images.

2.7 | Statistical analysis

Statistical tests were performed using MATLAB with significance level set at $p < 0.05$. Unless otherwise stated, inbuilt functions were used. All custom functions were obtained from files published on MATLAB File Exchange (https://uk.mathworks.com/matlabcentral/fileexchange). Normality was analyzed using the Shapiro-Wilk test (v1.1 by Ahmed BenSaïda). Levene's test was employed to assess homogeneity of variances. Data were analyzed using Welch's analysis of variance (ANOVA) test (v1.1 by Antonio Trujillo-Ortiz), followed by Games-Howell post hoc analysis (v1.1 by Pierre Mégevand).

3 | RESULTS AND DISCUSSION

3.1 | Edge intersection and floating island corrections

Small-world networks can be generated using a variety of approaches, but they have mostly been used for graph analysis, rather than physicalisation.[19,21,31,40] In this study, we generated lymph node-inspired, 3D printable small-world networks using a soft RGG model previously employed by Soekarjo et al. to model FRC networks.[31] While the model per se can recapitulate FRC network characteristics, it

needs to be modified for the generated networks to physicalize. In particular, the original model does not consider the physical sizes of nodes and edges—it only accounts for node-to-node distances. This is justified in the case of [31] because 3D printing was not their objective. However, it presents a limitation in the current work, as edges could form even in the presence of spatial obstruction by pre-existing nodes or edges (Figure 3). This could lead to edge intersections (known as edge crossings in graph theory) at locations that are not the shared endpoints of edges in the graph and, therefore, appear as new nodes when 3D printed.

Edge intersections in 3D space are a known graph embedding problem.[41] Recent efforts to resolve this technical challenge often involve incorporating non-crossing conditions.[42] In this work, we created a simple heuristic, which imposed an edge-to-edge proximity threshold (5 μm) forbidding edges that were either too close or intersecting each other (Figure 3A-B). To reduce computation time, the proximity check was performed on the network skeleton before it was skinned with a mesh. Although this means the actual gap space between individual struts could be less than 5 μm after meshing, the estimated pore size averaged across the image stack (mean $\pm$ SD) was 27 $\pm$ 9 μm (Video S5) and the thickness (mean $\pm$ SD) of struts in the mesh model was approximately 3 $\pm$ 1 μm (Video S6). Here, the thickness is only an approximate value because the 3D model had to be voxelised prior to the thickness analysis. It was, therefore, difficult to guarantee that the geometry of every part of the original model would voxelise well at a particular resolution. As a result, gaps of a few microns could form in the voxelised model. Taking that into account, it was decided to add a buffer distance, making it up to 5 μm. This, however, is not a fixed rule and could be adjusted depending on the scaffold size. Furthermore, the imposed proximity constraint successfully identified and removed all (in this case, three) edge intersections, as evident in both the CAD and SLS-printed models (Figure 3D-F).

Because nodes were positioned at random, it was often the case that insufficient nodes were initialized at the substrate surface for firm anchorage of the scaffold (Figure 4A). Depicted in Figure 4B is a scaffold that was formed approximately > 5.5 μm above the x-y plane, which, in its current state, would be unprintable. To remedy this, we used the Grasshopper plugin, FlexHopper, to simulate falling of the scaffold until it contacted the x-y plane and reached static equilibrium (Figure 4C). Another challenge came in the form of floating islands present in the structure (Figure 4D; Video S4). As the Nanoscribe system requires structures to be printed in an upside-down fashion, any floating islands would just float away in precursors that had not been polymerized. To correct for this, we created an algorithmic pipeline to scan the scaffold for floating islands (defined as isolated meshes above z = 0) and pull the detected islands down to the x-y plane (Figure 4E).

3.2 | Network analysis and topological characterization

Our desired number of edges (graph size) for 65 nodes used in network generation was 253. This was estimated from the average number of

FIGURE 3 (A) Rhino/Grasshopper model: sampling points placed on one of the edges. (B) Procedure of edge proximity detection and edge intersection removal. (C) Photograph of an SLS-printed scaffold next to a 25 mm × 25 mm substrate decorated with a 5 × 5 array of the same scaffold, fabricated using 2PP DLW (appears as white "dot" in the center). The scaffold was generated using $m = 80$ and $k = 40$ in the model. (D) Spatial network of the same scaffold. Purple circles represent nodes. Grey lines represent edges between the nodes. Purple lines represent intersecting edges that were removed by the algorithm. (E) Removed edges and their lengths. (F) Side-by-side comparison of CAD model and SLS-printed model, before (original) and after (modified) edge intersection correction. Arrows indicate points of intersections. Purple-colored regions indicate edges that were removed. Note that, relative to the CAD model, the SLS-model might appear thicker due to a wrapping operation that was applied to make the structure more robust to SLS printing and subsequent cleaning.
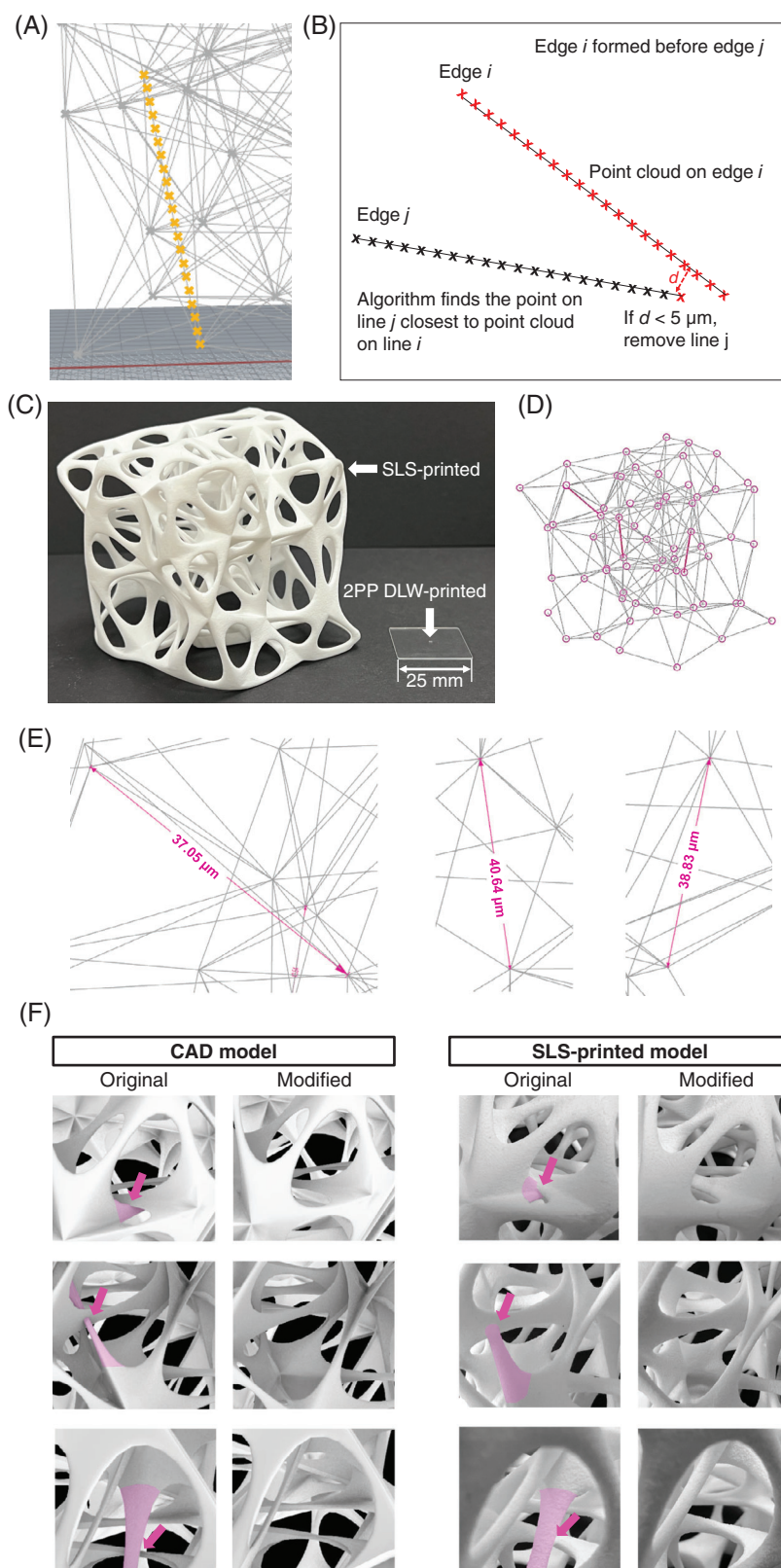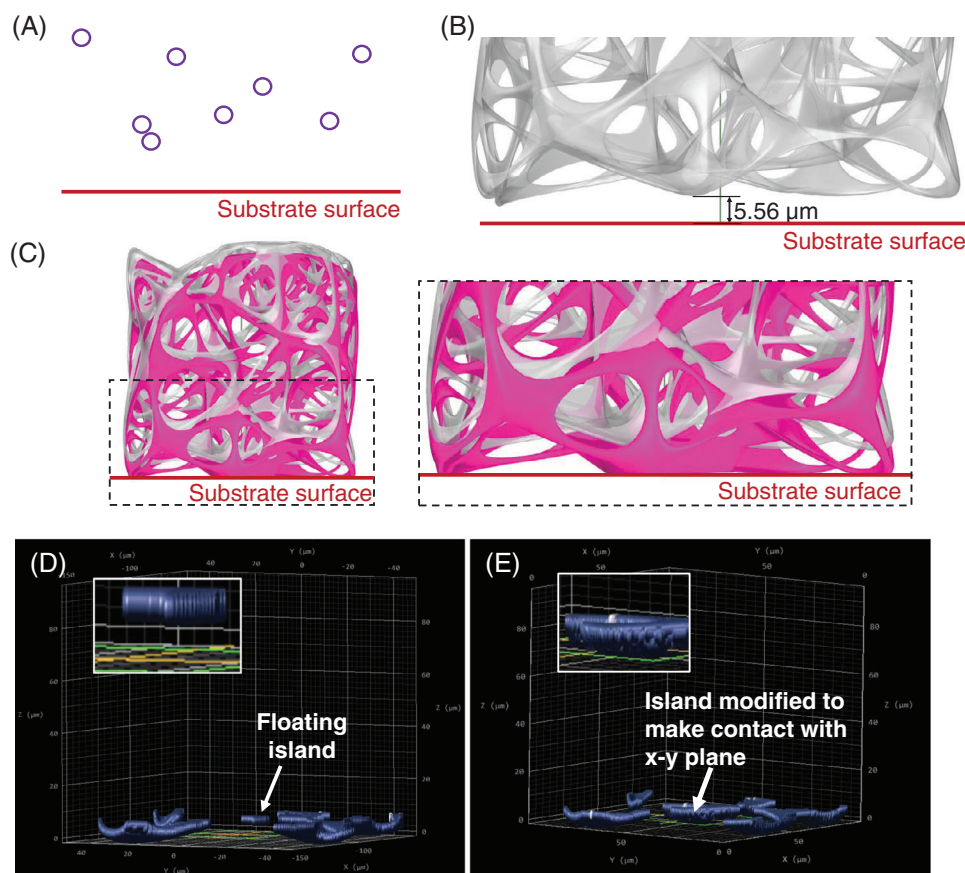
FIGURE 4 Correcting for substrate-contact and floating-island artefacts. (A) The random positioning of nodes meant that nodes forming the base of the scaffold were initialized above the x-y plane (equivalent to the substrate surface in 3D printing). (B) The random node positioning and connection resulted in a structure that was above the substrate surface and contained floating island artefacts. (C+D) The issues were mitigated by dropping the scaffold on the surface to increase the number of contact points and pulling the floating island down. Grey = old scaffold before artefact correction. Purple = new scaffold after artefact correction. One of the floating islands is more clearly visualized in (D), which shows the DeScribe interface. (E) The floating island artefact was removed after the modification.

edges per node (685 edges/176 nodes = 3.89 edges/node) and multiplied by the 65 nodes used in the current study. We aimed, therefore, to generate networks within 10% of the desired size: 253 ± 25 edges. This could be achieved by adjusting the combination of m and k values in the graph model. However, as intersecting edges were removed by our algorithm, it was important to inspect the graph size before and after the removal.

A parameter sweep revealed that values of $k > 40$ would initially generate > 340 edges, but this was reduced to ~300 edges after correcting for edge intersection (Figure S1; Table S3-4). Here, we identified that $k = 40$ (with m in the range: 20–80) was sufficient to generate networks of the target graph size. Moreover, it was found that the number of edges is more sensitive to k than to m (Figure S2). Thus, graphs generated with $m = 80$ were selected for further analysis to see how changes in k could affect the degree and physical edge length distributions. The distributions showed that high-degree nodes (Figure 5A) and physically long edges (Figure 5B) were suppressed as a result of the spatial constraints we imposed on the network. Moreover, an increase in k resulted in more high-degree nodes and long edges. This was expected, as k determines the node-node distance at which the

probability for connection, $p(d)$, is half-maximal. Nevertheless, longer edges also tend to have a higher chance of intersecting other edges, which explains why the distributions shifted to the left after correcting for edge intersections. This is reinforced by the fact that the three removed edges in the printed scaffold shown in Figure 3 were long edges (for $k = 40$) with lengths ~37 to 41 μm (Figure 3E).

We then asked how the edge intersection correction impacted small-worldness. Watts and Strogatz defined small-world networks as those with a high clustering coefficient relative to that of a random network and a low average shortest path length relative to that of a lattice network.[19] Therefore, we compared the generated networks ($m = 80$, $k = 40$) with benchmark networks—Watts-Strogatz small-world network (WS), Erdős-Rényi random network (ER) and lattice network (L) (Figure 6). We found that removing intersecting edges did not result in any significant difference between the original network (O) and modified network (M) in average local clustering coefficient, average shortest path length, and small-worldness (ω and SWP). Both O and M networks were topologically similar to FRC networks, as they exhibited lattice-like, small-world properties ($-0.5 < \omega < 0$) and fell within the "strong" small-world regime (SWP > 0.7).[28,31] Although the
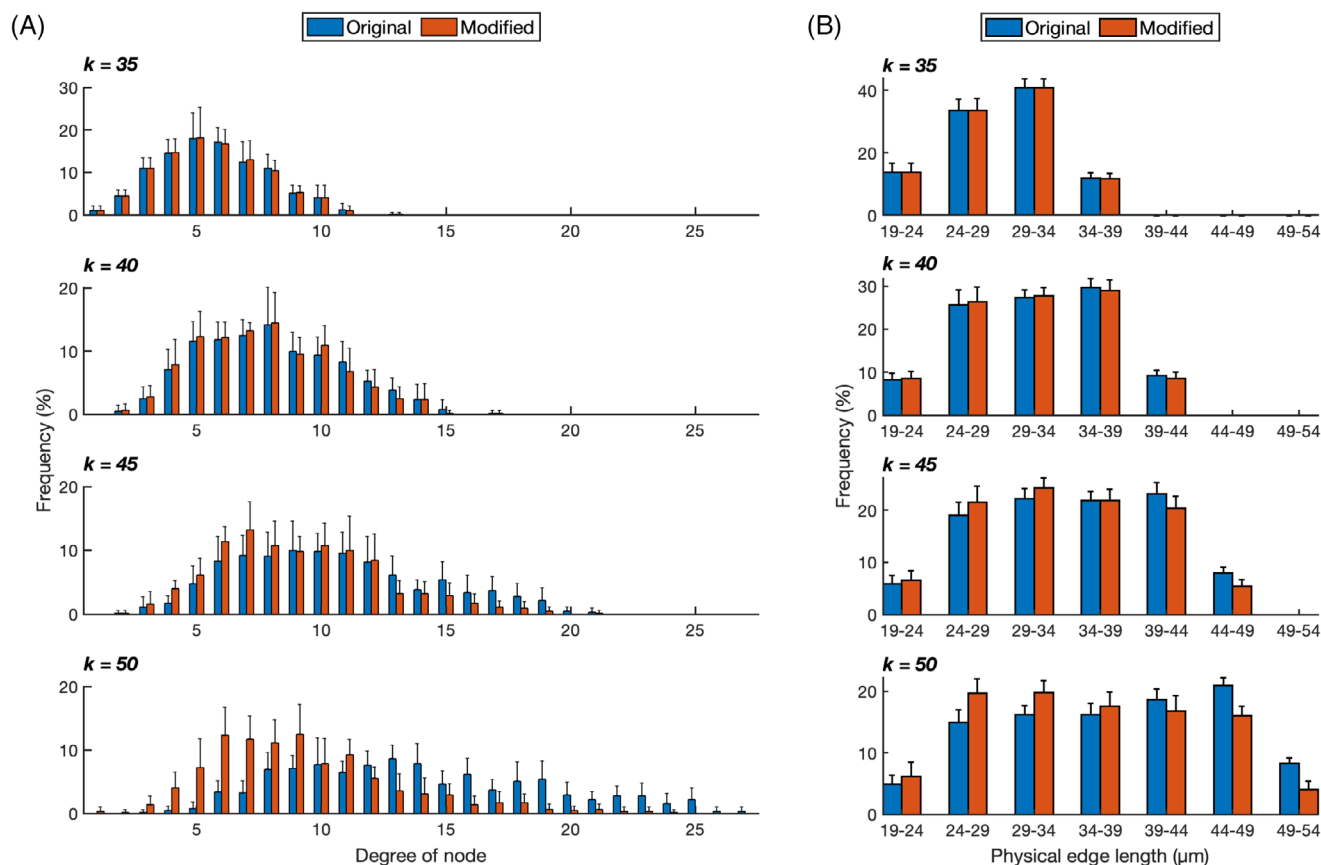
FIGURE 5 Distributions of (A) node degree (number of edges connected to a node) and (B) physical edge lengths before (original) and after (modified) correcting for intersecting edges. Results correspond to networks generated using $m = 80$ and $k = 35$–50. Data = mean $\pm$ SD ($N = 10$ simulations).

commonly used σ index was also computed for our networks (Table S3-4), it compares both the clustering coefficient and average path length to the same (random) graph and, therefore, does not capture how similar the test network is to a lattice network.[43]

Bars = mean $\pm$ SD ($N = 10$ simulations). Points = results from individual simulations. Statistical analysis was conducted using Welch's ANOVA, followed by Games-Howell post hoc test. $*p < 0.05$; $**p < 0.01$; NS—not significant.

3.3 | Microarchitected 3D scaffolds

We used 2PP DLW to 3D microprint one of the modified small-world scaffolds ($\omega = -0.10$ and SWP = 0.75). When the laser power (LP) was set at 100%, the Nanoscribe 3D printer was factory-calibrated to deliver a laser beam at 50 mW entering the aperture of the 63× objective. For optimization, we printed the scaffold using different LPs, ranging from 40% (20 mW) to 85% (43 mW) (Figure 7A). Here, it should be emphasized that the LP received by the resin was likely lower than that entering the objective, due to losses along the beam path.[44] We found that a LP ≤ 70% (35 mW) would result in structural deformation of the scaffold. Tilted views of scaffold arrays also revealed that many of the scaffolds had various degrees of collapse at LP < 70% (35 mW)

(Figure S3). At 40% (20 mW), the scaffold detached and only part of the base remained (Figure 7A). The observed structural distortions resemble those observed in other studies where lower LPs led to insufficient polymerization and mechanical instability.[44,45] Based on the optimization results, it was decided to fabricate 3D cell scaffolds using a LP level of 85% (43 mW), which closely resembled the CAD model (Figure 7B). The scaffolds were fabricated as 5 × 5 arrays on fused silica slides, which were successfully integrated with MatTek culture dishes (Figure 7C-D). Furthermore, top-down and tilted microscopy images confirmed the absence of structural collapse (Figure 7E-F).

3.4 | 3D cell culture and scaffold biocompatibility

A preliminary study was conducted to demonstrate the biocompatibility of the 3D microprinted scaffolds and visualize cell-scaffold interaction in 3D culture. Live cell imaging of FRCs on day 3 showed that they were able to adhere to the scaffold (Figure 8A). In addition, we observed scaffold autofluorescence, which is a known property of the resin, IP-Dip.[46] While this allowed for the simultaneous visualization of scaffolds and cells, it could hinder future analysis of the morphology, connectivity, or number of adhered cells. Such issue could potentially be mitigated by using a low-autofluorescence resin, such as IP-Visio
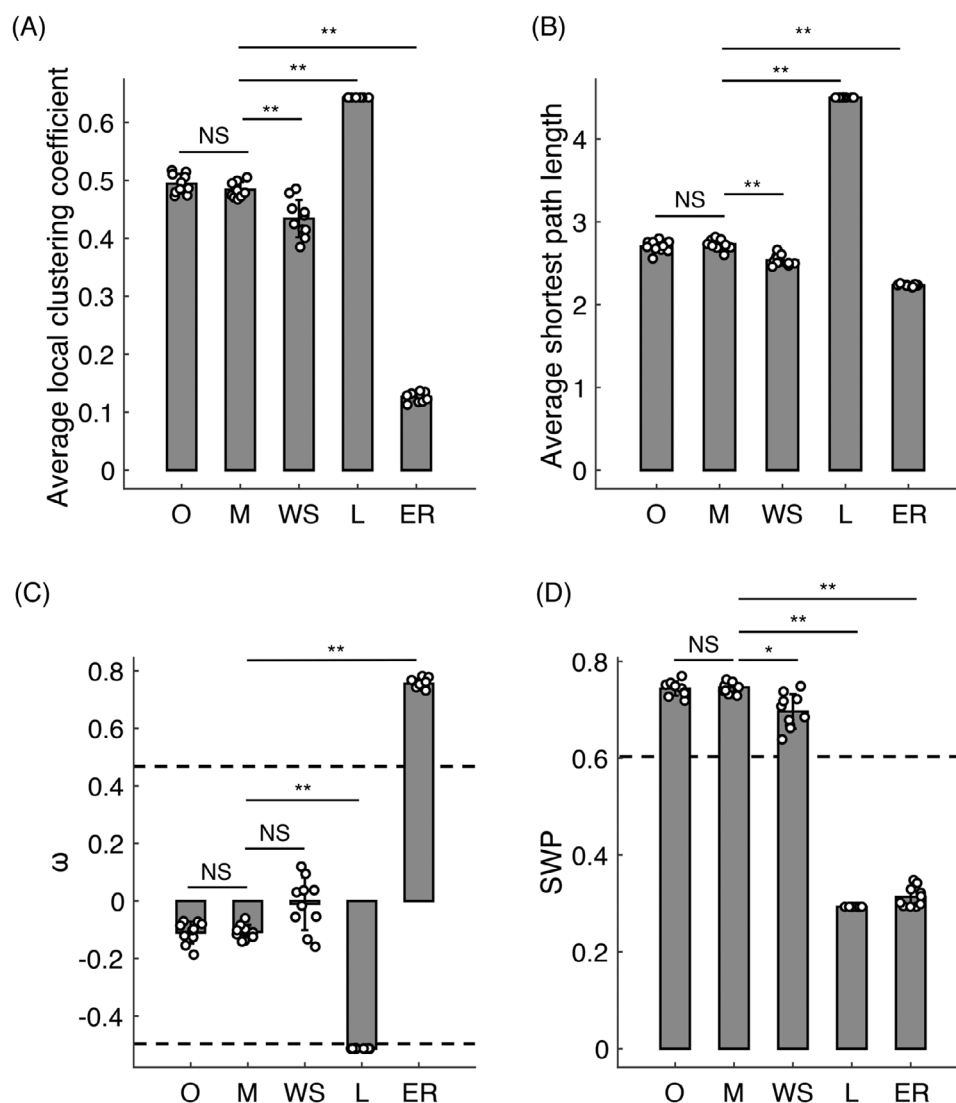
FIGURE 6 Comparison of topological parameters between the original network (O), modified network (M), as well as equivalent networks—Watts-Strogatz network (WS), ring lattice network (L) and Erdős-Rényi random network (ER). (A) Average local clustering coefficient. (B) Average shortest path length. (C) Omega factor (ω). Region bounded by dashed lines ($-0.5 < \omega < 0.5$) represents the small-world regime. (D) small-world propensity (SWP). Dashed line at SWP = 0.6 represents the threshold above which networks are considered to be in the "strong" small-world regime.

(Nanoscribe). Nevertheless, additional optimization of printing conditions would be required as IP-Visio is typically used for fabricating larger structures.

Although the focus of this work is scaffold topology, future designs could also incorporate morphology as a consideration, given its importance in modulating cell mechanics and mechanobiology.[47] Some of the FRCs on day 4 infiltrated the scaffold and conformed to the underlying morphology (Figure 8B). Visualization of F-actin cytoskeleton showed stress fiber alignment with some of the scaffold struts. This warrants future investigation into the extent to which 3D-cultured FRC networks could follow the underlying geometry (morphology and topology) of the scaffold network. It should be noted that the cell migration and infiltration required for network formation would likely depend on a multitude of factors, including porosity and

curvature.[48,49] Here, a porosity of $> 95\%$ was calculated for our scaffold model (Figure S6A), which is higher than that of many 3D printed cell scaffolds in tissue engineering.[50,51] Regarding scaffold curvature, we used Catmull-Clark subdivision to smoothen the scaffold mesh in Grasshopper (Figure S6B-E), but little is currently known about the effects of curvature on FRC network formation. Nevertheless, sharp changes in microscale curvature could mechanically induce cell membrane disruption, as demonstrated in NIH-3T3 fibroblasts.[52] Moreover, curvature could alter focal adhesions, cytoskeletal organization, and nuclear mechanics, which are known to modulate cell migration and differentiation.[51] Taken together, deeper study would be required to quantify the spatial distribution of cells throughout the scaffold and understand the biological impact of various physical factors.
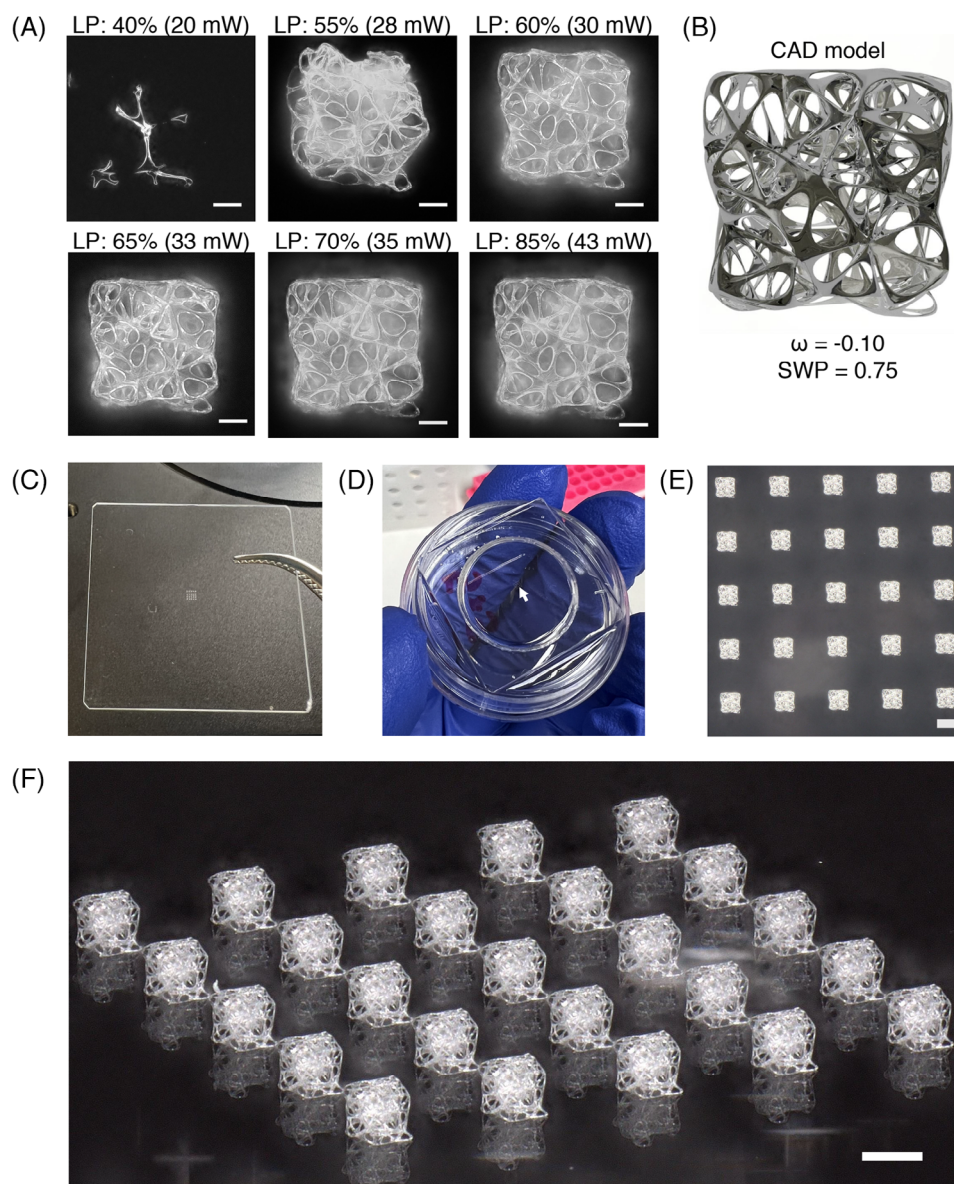
FIGURE 7 (A) Representative images of small-world 3D scaffolds fabricated using different levels of laser power (LP). Scale bars = 20 μm. (B) The CAD model of the printed small-world scaffolds. ω = omega factor. SWP = small-world propensity. (C) Representative image of a fused silica glass slide (25 mm × 25 mm; thickness = 0.7 mm) featuring a 5 × 5 scaffold array in the middle. (D) Scaffold array integrated with a bottomless culture dish using PDMS. Arrow indicates location of the scaffold array. (E) Magnified view of the same array. Scale bar = 100 μm. (F) Tilted view of the array. Scale bar = 100 μm. .

In addition to 3D culture of FRCs, several other applications could be explored using this 3D cell culture platform. For example, the scaffolds could be re-designed to capture the topology of other biological networks, such as neural networks (for scaffold-based nerve regeneration [34]), or ECM networks (for tumor microenvironment studies [53,54]). However, it should be noted that topological characterization of biological structural networks outside of neuroscience is relatively sparse. We anticipate that, in parallel to advances in connectomics,[55] more data will become available (such as [27,28]) for the algorithmic design of scaffolds for non-neural cell culture. This would benefit not only tissue engineering,[5] but also cancer and immunological

research—for instance, to study the effects of structural connectivity on chimeric antigen receptor (CAR) T cells in complex tumor-like microenvironments,[56] or how 3D structures could influence T cell-T cell communication and collective decisions.[57,58]

4 | CONCLUSION

We have developed a unique approach combining graph theory, algorithmic design and 2PP DLW to create microscale 3D cell scaffolds. In terms of geometric complexity and resolution, our approach
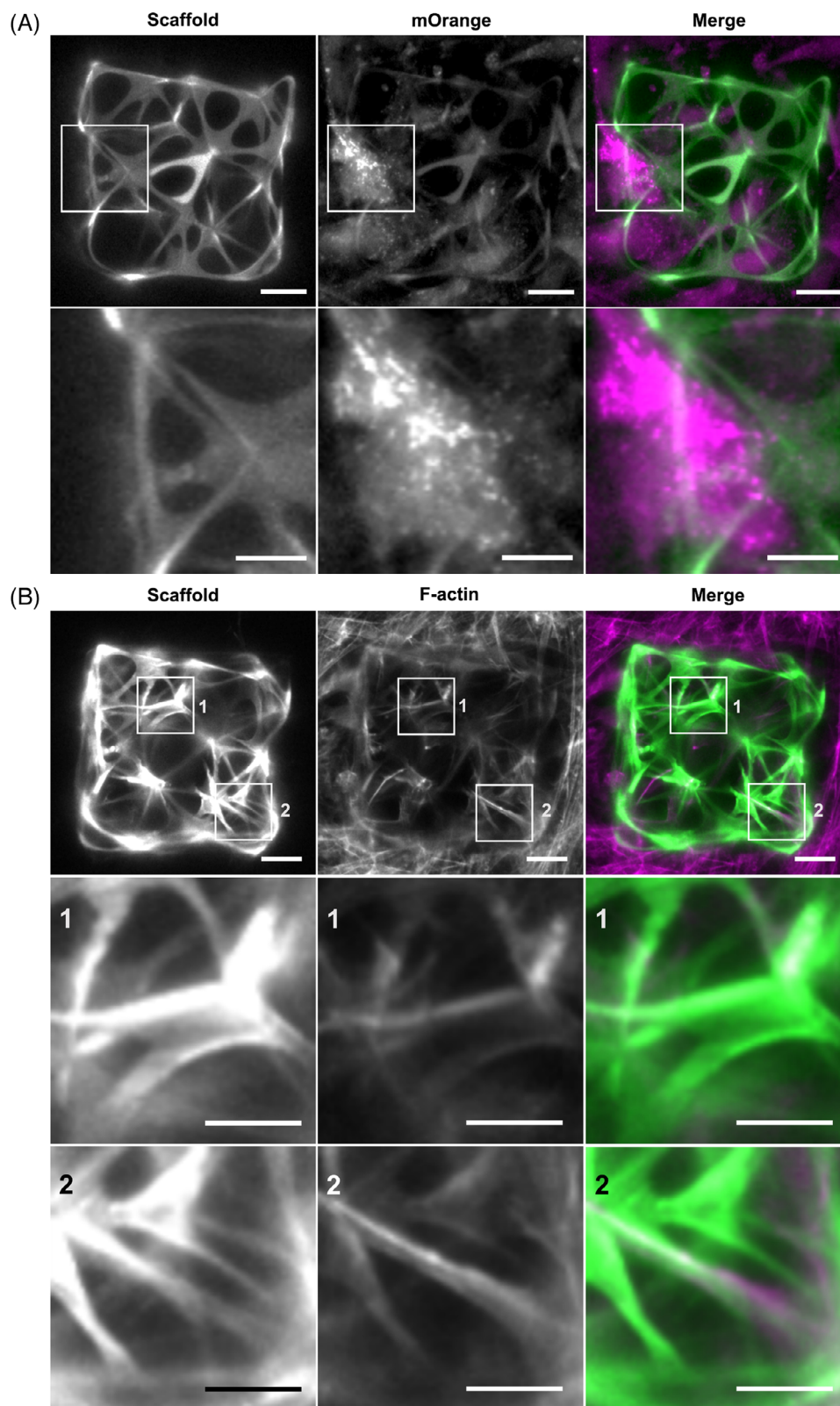
FIGURE 8 Representative confocal microscopy z-projection (sum of intensities) images of FRCs on 3D microprinted scaffolds. (A) Live-cell imaging was performed on day 3 post-seeding. Magenta = mOrange-labelled cells. Green = scaffold autofluorescence. Top row: scale bars = 20 μm. Bottom row: images represent magnified regions outlined in top row. Scale bars = 10 μm. (B) Images of fixed FRCs on day 4. Magenta = F-actin. Green = scaffold autofluorescence. Top row: scale bars = 20 μm. Middle + bottom rows: images represent magnified regions outlined in top row. Scale bars = 10 μm.

outperforms other current biomaterial-based models of FRC networks.[5] Previously, the task of generating FRC-like small-world networks was confined to computational modelling. Our innovative toolkit now extends this capability into the realm of biomaterials, physicalizing small-world networks through 3D microprinting. In the design process, we found that the original RGG model would generate networks with intersecting edges and floating islands. These issues were rectified using our Grasshopper-based algorithmic toolset, which placed additional spatial constraints on the generative process. Network analysis showed that the generated scaffolds possessed a lattice-like, small-world network topology ($\omega = -0.10 \pm 0.02$) which put them in the same topological classification as FRC networks. Optimization of 2PP DLW revealed that a high laser power (> 70%; 35 mW) was required to ensure adequate polymerization and prevent structural collapse of the scaffolds. As a proof-of-concept, our 3D cell culture study showed that the scaffolds supported the survival and infiltration of FRCs. Overall, this has demonstrated how graph theory can be utilized, not only in histological analysis or in silico modelling, but also as a bioinspired design principle to drive the development of cell scaffolds. Going beyond simple structures, this approach enables the creation of 3D scaffolds recapitulating topological properties of biologically relevant complex networks. Combined with the ability to fabricate at the microscale, this culture platform could open new lines of enquiry related to major challenges in cancer immunotherapies and fundamental mechanisms in cell mechanobiology. In the future, these topologically representative scaffolds could also be utilized in preclinical settings to support the culture of delicate patient-derived tumor explants via provision of appropriate geometric and mechanical properties, as well as ECM components.[59]

AUTHOR CONTRIBUTION

Matthew Chin: Conceptualization, Data curation, Formal analysis, Investigation, Methodology, Software, Validation, Visualization, Writing – original draft. **Barry Reid**: Investigation, Resources. **Veronika Lachina**: Investigation, Writing – original draft. **Sophie Acton**: Resources, Supervision, Writing – review & editing. **Marc-Olivier Coppens**: Conceptualization, Funding acquisition, Methodology, Project administration, Resources, Supervision, Writing – review & editing. Matthew H. W. Chin: Conceptualization; Data curation; Formal analysis; Investigation; Methodology; Visualization; Writing – original draft; Writing – review & editing. Barry Reid: Data curation; Investigation. Veronika Lachina: Data curation; Investigation; Writing – original draft; Writing – review & editing. Sophie E. Acton: Funding acquisition; Investigation; Resources; Visualization; Writing – review & editing. Marc-Olivier Coppens: Conceptualization; Formal analysis; Funding acquisition; Investigation; Methodology; Project administration; Resources; Supervision; Writing – review & editing

CONFLICT OF INTEREST STATEMENT

The authors declare no conflict of interest.

DATA AVAILABILITY STATEMENT

The data that supports the findings of this study are available in the supplementary material of this article. The algorithm for scaffold generation is available on GitHub (https://github.com/mattychin/3D-cell-scaffold-generator).

ORCID

Matthew H. W. Chin https://orcid.org/0000-0003-1633-7786
Barry Reid https://orcid.org/0000-0002-4803-829X
Sophie E. Acton https://orcid.org/0000-0003-2704-716X
Marc-Olivier Coppens https://orcid.org/0000-0002-1810-2537

REFERENCES

1. Loh, Q. L., & Choong, C. (2013). Three-dimensional scaffolds for tissue engineering applications: Role of porosity and pore size. *Tissue Engineering Part B Reviews*, *19*, 485. https://doi.org/10.1089/TEN.TEB.2012.0437

2. Echeverria Molina, M. I., Malollari, K. G., & Komvopoulos, K. (2021). Design challenges in polymeric scaffolds for tissue engineering. *Frontiers in Bioengineering and Biotechnology*, *9*, 231. https://doi.org/10.3389/FBIOE.2021.617141/XML/NLM

3. Valdoz, J. C., Johnson, B. C., Jacobs, D. J., Franks, N. A., Dodson, E. L., Sanders, C., Cribbs, C. G., & van Ry, P. M. (2021). The ECM: To scaffold, or not to scaffold, that is the question. *International Journal of Molecular Sciences*, *22*, https://doi.org/10.3390/IJMS222312690

4. Fletcher, A. L., Acton, S. E., & Knoblich, K. (2015). Lymph node fibroblastic reticular cells in health and disease. *Nature Reviews Immunology*, *15*, 350–361. https://doi.org/10.1038/nri3846

5. Shou, Y., Johnson, S. C., Quek, Y. J., Li, X., & Tay, A. (2022). Integrative lymph node-mimicking models created with biomaterials and computational tools to study the immune system. *Materials Today Biology*, *14*, https://doi.org/10.1016/J.MTBIO.2022.100269

6. Zhao, P., Gu, H., Mi, H., Rao, C., Fu, J., & Turng, L. (2017). Fabrication of scaffolds in tissue engineering: A review. *Frontiers of Mechanical Engineering*, 2018 13:1. 13 107–119. https://doi.org/10.1007/S11465-018-0496-8

7. Huang, G., Li, F., Zhao, X., Ma, Y., Li, Y., Lin, M., Jin, G., Lu, T. J., Genin, G. M., & Xu, F. (2017). Functional and biomimetic materials for engineering of the three-dimensional cell microenvironment. *Chemical Reviews*, *117*, 12764. https://doi.org/10.1021/ACS.CHEMREV.7B00094

8. Coburn, J., Gibson, M., Bandalini, P. A., Laird, C., Mao, H. Q., Moroni, L., Seliktar, D., & Elisseeff, J. (2011). Biomimetics of the extracellular matrix: An integrated three-dimensional fiber-hydrogel composite for cartilage tissue engineering. *Smart Structures and Systems*, *7*, 213–222. https://doi.org/10.12989/sss.2011.7.3.213

9. LaFratta, C. N., Fourkas, J. T., Baldacchini, T., & Farrer, R. A. (2007). Multiphoton fabrication. *Angewandte Chemie International Edition*, 46, 6238–6258. https://doi.org/10.1002/ANIE.200603995

10. Hu, Q., Sun, X. Z., Parmenter, C. D. J., Fay, M. W., Smith, E. F., Rance, G. A., He, Y., Zhang, F., Liu, Y., Irvine, D., Tuck, C., Hague, R., & Wildman, R. (2017). Additive manufacture of complex 3D Au-containing nanocomposites by simultaneous two-photon polymerisation and photoreduction. *Scientific Reports*, 2017 7:1. 7, 1–9. https://doi.org/10.1038/s41598-017-17391-1

11. Maggi, A., Li, H., & Greer, J. R. (2017). Three-dimensional nano-architected scaffolds with tunable stiffness for efficient bone tissue growth. *Acta Biomaterialia*, 63, 294. https://doi.org/10.1016/J.ACTBIO.2017.09.007

12. Meza, L. R., Das, S., & Greer, J. R. (2014). Strong, lightweight, and recoverable three-dimensional ceramic nanolattices. *Science*, 345(6202), 1322–1326. https://doi.org/10.1126/SCIENCE.1255908/SUPPL_FILE/MEZA.SM.PDF

13. Liu, Y., Wang, H., Ho, J., Ng, R. C., Ng, R. J. H., Hall-Chen, V. H., Koay, E. H. H., Dong, Z., Liu, H., Qiu, C. W., Greer, J. R., & Yang, J. K. W. (2019). Structural color three-dimensional printing by shrinking photonic crystals. *Nature Communications*, 2019 10:1. 10, 1–8. https://doi.org/10.1038/s41467-019-12360-w

14. Lemma, E. D., Spagnolo, B., De Vittorio, M., & Pisanello, F. (2019). Studying cell mechanobiology in 3D: The two-photon lithography approach. *Trends in Biotechnology*, 37, 358–372. https://doi.org/10.1016/j.tibtech.2018.09.008

15. Mirzaali, M. J., Pahlavani, H., & Zadpoor, A. A. (2019). Auxeticity and stiffness of random networks: Lessons for the rational design of 3D printed mechanical metamaterials. *Applied Physics Letters*, 115, 021901. https://doi.org/10.1063/1.5096590

16. Carleton, J. B., D'Amore, A., Feaver, K. R., Rodin, G. J., & Sacks, M. S. (2015). Geometric characterization and simulation of planar layered elastomeric fibrous biomaterials. *Acta Biomaterialia*, 12, 93–101. https://doi.org/10.1016/J.ACTBIO.2014.09.049

17. Hatami-Marbini, H., & Rohanifar, M. (2021). Nonlinear mechanical properties of prestressed branched fibrous networks. *Biophysical Journal*, 120, 527. https://doi.org/10.1016/J.BPJ.2020.10.050

18. Ruiz-Franco, J., & van der Gucht, J. (2022). Force transmission in disordered fibre networks. *Frontiers in Cell and Developmental Biology*, 10, https://doi.org/10.3389/FCELL.2022.931776/FULL

19. Watts, D. J., & Strogatz, S. H. (1998). Collective dynamics of "small-world" networks. *Nature*, 393, 440–442. https://doi.org/10.1038/30918

20. Bullmore, E., & Sporns, O. (2012). The economy of brain network organization. *Nature Reviews Neuroscience*, 2012 13:5. 13, 336–349. https://doi.org/10.1038/nrn3214

21. Barthelemy, M. (2018). Random geometric graphs. in: *Morphogenesis of spatial networks. lecture notes in morphogenesis.*, Springer, Cham: pp. 177–196. https://doi.org/10.1007/978-3-319-20565-6_9

22. Bassett, D. S., & Bullmore, E. T. (2017). Small-world brain networks revisited. *The Neuroscientist*, 23, 499–516. https://doi.org/10.1177/1073858416667720/ASSET/IMAGES/LARGE/10.1177_1073858416667720-FIG2.JPEG

23. Gunduz, C., Yener, B., & Gultekin, S. H. (2004). The cell graphs of cancer. *Bioinformatics*, 20, i145–i151. https://doi.org/10.1093/bioinformatics/bth933

24. Failmezger, H., Muralidhar, S., Rullan, A., de Andrea, C. E., Sahai, E., & Yuan, Y. (2020). Topological tumor graphs: A graph-based spatial model to infer stromal recruitment for immunosuppression in melanoma histology. *Cancer Research*, 256, 1199–1209. https://doi.org/10.1158/0008-5472.CAN-19-2268

25. Kollmannsberger, P., Kerschnitzki, M., Repp, F., Wagermaier, W., Weinkamer, R., & Fratzl, P. (2017). The small world of osteocytes: Connectomics of the lacuno-canalicular network in bone. *New Journal of Physics*, 19, 73019. https://doi.org/10.1088/1367-2630/aa764b

26. Muldoon, S. F., Bridgeford, E. W., & Bassett, D. S. (2016). Small-world propensity and weighted brain networks. *Scientific Reports*, 6, https://doi.org/10.1038/SREP22057

27. Novkovic, M., Onder, L., Bocharov, G., & Ludewig, B. (2020). Topological structure and robustness of the lymph node conduit system. *Cell Reports*, 30, 893–904.e6. https://doi.org/10.1016/j.celrep.2019.12.070

28. Novkovic, M., Onder, L., Cupovic, J., Abe, J., Bomze, D., Cremasco, V., Scandella, E., Stein, J. v., Bocharov, G., Turley, S. J., & Ludewig, B. (2016). Topological small-world organization of the fibroblastic reticular cell network determines lymph node functionality. *PLoS Biology*, 14, e1002515. https://doi.org/10.1371/journal.pbio.1002515

29. Kochenderfer, J. N., Dudley, M. E., Kassim, S. H., Somerville, R. P. T., Carpenter, R. O., Maryalice, S. S., Yang, J. C., Phan, G. Q., Hughes, M. S., Sherry, R. M., Raffeld, M., Feldman, S., Lu, L., Li, Y. F., Ngo, L. T., Goy, A., Feldman, T., Spaner, D. E., Wang, M. L., & Rosenberg, S. A. (2015). Chemotherapy-refractory diffuse large B-cell lymphoma and indolent B-cell malignancies can be effectively treated with autologous T cells expressing an anti-CD19 chimeric antigen receptor. *Journal of Clinical Oncology*, 33, 540–549. https://doi.org/10.1200/JCO.2014.56.2025

30. Coppens, M.-O. (2021). Nature-inspired chemical engineering for process intensification. *Annual Review of Chemical and Biomolecular Engineering*, 12, 187–215. https://doi.org/10.1146/annurev-chembioeng-060718-030249

31. Soekarjo, K. M. W., Textor, J., & de Boer, R. J. (2019). Local attachment explains small world–like properties of fibroblastic reticular cell networks in lymph nodes. *Journal of Immunology*, 202, 3318–3325. https://doi.org/10.4049/jimmunol.1801016

32. Bajénoff, M., Egen, J., Koo, L. Y., Laugier, J. P., Brau, F., Glaichenhaus, N., & Germain, R. N. (2006). Stromal cell networks regulate lymphocyte entry, migration, and territoriality in lymph nodes. *Immunity*, 25, 989. https://doi.org/10.1016/J.IMMUNI.2006.10.011

33. Oakdale, J. S., Ye, J., Smith, W. L., & Biener, J. (2016). Post-print UV curing method for improving the mechanical properties of prototypes derived from two-photon lithography. *Optics Express*, 24, 27077. https://doi.org/10.1364/OE.24.027077

34. Agrawal, L., Saidani, M., Guillaud, L., & Terenzio, M. (2021). Development of 3D culture scaffolds for directional neuronal growth using 2-photon lithography. *Materials Science and Engineering: C*, 131, 112502. https://doi.org/10.1016/J.MSEC.2021.112502

35. Telesford, Q. K., Joyce, K. E., Hayasaka, S., Burdette, J. H., & Laurienti, P. J. (2011). The ubiquity of small-world networks. *Brain Connect*, 1, 367. https://doi.org/10.1089/BRAIN.2011.0038

36. Maslov, S., & Sneppen, K. (2002). Specificity and stability in topology of protein networks. *Science*, 296, 910–913. https://doi.org/10.1126/SCIENCE.1065103

37. Sporns, O., & Zwi, J. D. (2004). The small world of the cerebral cortex. *Neuroinformatics*, 2, 145–162. https://doi.org/10.1385/NI:2:2:145/METRICS

38. Erdös, P., & Rényi, A. (1959). On random graphs I. *Publicationes Mathematicae Debrecen*, 6, 290.

39. Acton, S. E., Farrugia, A. J., Astarita, J. L., Mourão-Sá, D., Jenkins, R. P., Nye, E., Hooper, S., Van Blijswijk, J., Rogers, N. C., Snelgrove, K. J., Rosewell, I., Moita, L. F., Stamp, G., Turley, S. J., Sahai, E., & Sousa, C. R. (2014). Dendritic cells control fibroblastic reticular network tension and lymph node expansion. *Nature*, 514, 498–502. https://doi.org/10.1038/nature13814

40. Onesto, V., Accardo, A., Vieu, C., & Gentile, F. (2020). Small-world networks of neuroblastoma cells cultured in three-dimensional polymeric scaffolds featuring multi-scale roughness. *Neural Regen Research*, 15, 759. https://doi.org/10.4103/1673-5374.266923

41. Dujmović, V., & Whitesides, S. (2013). Three-dimensional drawings. in: R. Tamassia (Ed.), *Handbook of graph drawing and visualization (Discrete Mathematics and Its Applications)*, Chapman & Hall/CRC: pp. 455–488.

42. Dehmamy, N., Milanlouei, S., & Barabási, A. L. (2018). A structural transition in physical networks. *Nature*, 2018 563:7733. 563, 676–680. https://doi.org/10.1038/s41586-018-0726-6

43. Neal, Z. P. (2017). How small is it? Comparing indices of small worldliness. *Network Science*, 5, 30–44. https://doi.org/10.1017/NWS.2017.5

44. Hengsbach, S., & Lantada, A. D. (2014). Direct laser writing of auxetic structures: Present capabilities and challenges. *Smart Materials and Structures*, 23, 085033. https://doi.org/10.1088/0964-1726/23/8/085033

45. Oakdale, J. S., Smith, W. L., Biener, J., Zhou, X., Hou, Y., Lin, J., Peng, S., Zhang, R., Chen, V. H., Khabiboulline, E. T., Braun, P., & Atwater, H. A. (2016). Post-print UV curing method for improving the mechanical properties of prototypes derived from two-photon lithography. *Optics Express*, 24(24), 27077–27086. https://doi.org/10.1364/OE.24.027077

46. Lamont, A. C., Lamont, A. C., Lamont, A. C., Lamont, A. C., Restaino, M. A., Restaino, M. A., Restaino, M. A., Alsharhan, A. T., Alsharhan, A. T., Alsharhan, A. T., Liu, Z., Hammer, D. X., Sochol, R. D., Sochol, R. D., Sochol, R. D., & Agrawal, A. (2020). Direct laser writing of a titanium dioxide-laden retinal cone phantom for adaptive optics-optical coherence tomography. *Optical Materials Express*, 10, 2757–2767. https://doi.org/10.1364/OME.400450

47. Han, P., Gomez, G. A., Duda, G. N., Ivanovski, S., & Poh, P. S. P. (2022). Scaffold geometry modulation of mechanotransduction and its influence on epigenetics. *Acta Biomaterialia*, https://doi.org/10.1016/J.ACTBIO.2022.01.020

48. Song, K. H., Park, S. J., Kim, D. S., & Doh, J. (2015). Sinusoidal wavy surfaces for curvature-guided migration of T lymphocytes. *Biomaterials*, 51, 151–160. https://doi.org/10.1016/J.BIOMATERIALS.2015.01.071

49. Pieuchot, L., Marteau, J., Guignandon, A., Dos Santos, T., Brigaud, I., Chauvy, P. F., Cloatre, T., Ponche, A., Petithory, T., Rougerie, P., Vassaux, M., Milan, J. L., Tusamda Wakhloo, N., Spangenberg, A., Bigerelle, M., & Anselme, K. (2018). Curvotaxis directs cell migration through cell-scale curvature landscapes. *Nature Communications*, 2018 9:1. 9, 1–13. https://doi.org/10.1038/s41467-018-06494-6

50. Poh, P. S. P., Valainis, D., Bhattacharya, K., van Griensven, M., & Dondl, P. (2019). Optimization of bone scaffold porosity distributions. *Scientific Reports*, 9, 1–10. https://doi.org/10.1038/S41598-019-44872-2/FIGURES/6

51. Yang, Y., Xu, T., Bei, H. P., Zhang, L., Tang, C. Y., Zhang, M., Xu, C., Bian, L., Yeung, K. W. K., Fuh, J. Y. H., & Zhao, X. (2022). Gaussian curvature-driven direction of cell fate toward osteogenesis with triply periodic minimal surface scaffolds. *Proceedings National Academy of Science USA*, 119, e2206684119. https://doi.org/10.1073/PNAS.2206684119/SUPPL_FILE/PNAS.2206684119.SAPP.PDF

52. Capozza, R., Caprettini, V., Gonano, C. A., Bosca, A., Moia, F., Santoro, F., & De Angelis, F. (2018). Cell membrane disruption by vertical micro-/nanopillars: Role of membrane bending and traction forces. *ACS Appl Mater Interfaces*, 10, 29107–29114. https://doi.org/10.1021/ACSAMI.8B08218/ASSET/IMAGES/LARGE/AM-2018-08218X_0005.JPEG

53. Vicente-Munuera, P., Burgos-Panadero, R., Noguera, I., Navarro, S., Noguera, R., & Escudero, L. M. (2020). The topology of vitronectin: A complementary feature for neuroblastoma risk classification based on computer-aided detection. *International Journal of Cancer*, 146, 553. https://doi.org/10.1002/IJC.32495

54. Tadeo, I., Berbegall, A. P., Escudero, L. M., Álvaro, T., & Noguera, R. (2014). Biotensegrity of the extracellular matrix: Physiology, dynamic mechanical balance, and implications in oncology and mechanotherapy. *Frontiers in Oncology*, 4, https://doi.org/10.3389/FONC.2014.00039

55. Gosak, M., Milojević, M., Duh, M., Skok, K., & Perc, M. (2022). Networks behind the morphology and structural design of living systems. *Physics of Life Reviews*, 41, 1–21. https://doi.org/10.1016/J.PLREV.2022.03.001

56. Tabdanov, E. D., Rodríguez-Merced, N. J., Cartagena-Rivera, A. X., Puram, V. V., Callaway, M. K., Ensminger, E. A., Pomeroy, E. J., Yamamoto, K., Lahr, W. S., Webber, B. R., Moriarity, B. S., Zhovmer, A. S., & Provenzano, P. P. (2021). Engineering T cells to enhance 3D migration through structurally and mechanically complex tumor microenvironments. *Nature Communications*, 2021 12:1. 12, 1–17. https://doi.org/10.1038/s41467-021-22985-5

57. Gérard, A., Khan, O., Beemiller, P., Oswald, E., Hu, J., Matloubian, M., & Krummel, M. F. (2013). Secondary T cell–T cell synaptic interactions drive the differentiation of protective CD8+ T cells. *Nature Immunology*, 2013 14:4. 14, 356–363. https://doi.org/10.1038/ni.2547

58. Polonsky, M., Rimer, J., Kern-Perets, A., Zaretsky, I., Miller, S., Bornstein, C., David, E., Kopelman, N. M., Stelzer, G., Porat, Z., Chain, B., & Friedman, N. (2018). Induction of CD4 T cell memory by local cellular collectivity. *Science*, 1979, 360. https://doi.org/10.1126/science.aaj1853

59. Wu, K. Z., Adine, C., Mitriashkin, A., Aw, B. J. J., Iyer, N. G., & Fong, E. L. S. (2023). Making in vitro tumor models whole again. *Advanced Healthcare Materials*, 12, 2202279. https://doi.org/10.1002/adhm.202202279

SUPPORTING INFORMATION

Additional supporting information can be found online in the Supporting Information section at the end of this article.